J. Fluid Mech. (2009), *vol.* 630, *pp.* 43–69. © 2009 Cambridge University Press
doi:10.1017/S0022112009006879 Printed in the United Kingdom

Cylinders with square cross-section: wake instabilities with incidence angle variation

GREGORY J. SHEARD[1]†, MATTHEW J. FITZGERALD[2] AND KRIS RYAN[1]

[1]Fluids Laboratory for Aeronautical and Industrial Research (FLAIR), Department of Mechanical and Aerospace Engineering, Monash University, VIC 3800, Australia

[2]AMOG Consulting, Sea Technology House, 19 Business Park Drive, Monash Business Park, Notting Hill, VIC 3168, Australia

(Received 27 October 2008 and in revised form 9 March 2009)

The wakes behind square cylinders with variation in incidence angle are computed over a range of Reynolds numbers to elucidate the three-dimensional stability and dynamics up to a Reynolds number of $Re = 300$, based on the projected height of the inclined square cylinder. Three-dimensional instability modes are predicted and computed using a linear stability analysis technique and three-dimensional simulations, respectively. Depending on the incidence angle, the flow is found to transition to three-dimensional flow through either a mode A instability, or a subharmonic mode C instability. The mode A instability is predicted as the first-occurring instability at incidence angles smaller than 12° and greater than 26°, with the mode C instability predicted between these incidence angles. At a zero-degree angle of incidence, the wake instabilities closely match modes A, B and a quasi-periodic mode predicted in earlier studies behind square and circular cylinders. With increasing angle of incidence, the three-dimensional wake transition Reynolds number first increases from $Re = 164$ as the mode A instability weakens, before decreasing again beyond an incidence angle of 12° as the wake becomes increasingly unstable to the mode C instability, and then again to the mode A instability as the incidence angle approaches 45°. A spanwise autocorrelation analysis from computations over a cylinder span 20 times the square cross-section side length reveals that beyond the onset of three-dimensional instabilities, the vortex street breaks down with patterns consistent with spatio-temporal chaos. This effect was more pronounced at higher incidence angles.

1. Introduction

The transition from two- to three-dimensional flow around a bluff body is an important phenomenon to understand in an engineering context, as the wake-induced forces can have potentially detrimental structural or positional effects on the body or its surroundings. Lift and drag forces on bodies are altered by the development of three-dimensional structures in the wake (Thompson, Hourigan & Sheridan 1996), and structures that develop at the onset of three-dimensional transition have been observed to persist to Reynolds numbers as high as 10 000 (Mansy, Yang & Williams 1994). Understanding the behaviour of the wake at transition can inform the likely

† Email address for correspondence: Greg.Sheard@eng.monash.edu.au

https://doi.org/10.1017/S0022112009006879 Published online by Cambridge University Press

behaviour of the wake at higher Reynolds numbers, without resorting to expensive resolution of the turbulent wake.

The transitional behaviour of the wakes behind a number of bluff bodies has been the subject of extensive numerical and experimental investigation. For instance, Karniadakis & Triantafyllou (1992); Barkley & Henderson (1996); Thompson *et al.* (1996); Williamson (1996); Leweke & Williamson (1998); Thompson, Leweke & Williamson (2001*b*) investigated a circular cylinder, Sheard (2007) investigated an elliptical cylinder, Ryan, Thompson & Hourigan (2005) investigated an elongated cylinder and Robichaux, Balachandar & Vanka (1999); Sohankar, Norberg & Davidson (1999); Luo, Chew & Ng (2003); Saha, Biswas & Muralidhar (2003); Luo, Tong & Khoo (2007); Tong, Luo & Khoo (2008) investigated a cylinder with a square cross-section. A general consensus arising from these studies is that cylinder wakes may be unstable to two regular modes (modes A and B) with a unique spanwise wavelength and spatiotemporal symmetry. In addition, systems with a plane of symmetry through the wake centreline may also be unstable to a quasi-periodic mode, whereas systems without this symmetry also permit a subharmonic mode (sometimes referred to as mode C in the context of cylinder wakes; see Marques, Lopez & Blackburn 2004, for a detailed analysis of this behaviour). A subharmonic mode C instability was discovered in the wakes behind rings by Sheard, Thompson & Hourigan (2003); Sheard *et al.* (2005), and in a numerical investigation of staggered pairs of cylinders, Carmo *et al.* (2008) found evidence that mode C sometimes plays a prominent role in the bifurcation from two- to three-dimensional flow.

Square cylinders at an angle of incidence have received attention recently (Dutta, Panigrahi & Muralidhar 2008; Ranjan, Dalal & Biswas 2008), though the three-dimensional wake stability of these flows has largely focused on the zero-incidence-angle case (Robichaux *et al.* 1999; Sohankar *et al.* 1999; Luo *et al.* 2003; Saha *et al.* 2003; Luo *et al.* 2007). Only a very recent experimental study (Tong *et al.* 2008) has considered the impact of incidence angle variation on wake stability. Despite the absence of a reflective symmetry for square cylinders at inclination angles between 0° and 45° that study detected transitions attributed to modes A and B, and not a subharmonic mode. At a zero-incidence angle, Robichaux *et al.* (1999) predicted the critical Reynolds numbers for transition to modes A and B, as well as to a third instability mode resembling a subharmonic mode (their mode S), to be 162 ± 12, 190 ± 14 and 200 ± 5, respectively. The modes were observed to be most unstable to spanwise perturbations with wavelengths of $5.22d$, $1.2d$ and $2.8d$, respectively. These values compare favourably to other studies. For instance, (Luo *et al.* 2003) found through experimental measurements that these transitions occurred at approximately $Re = 160$ and 200, respectively.

In this study, a linear stability analysis is conducted with the support of three-dimensional computations to develop our understanding of the stability and dynamics of the wakes behind inclined square cylinders through the three-dimensional transition regime. In particular, the question as to the existence of a subharmonic mode in addition to modes A and B will be addressed.

The structure of this paper is as follows. In § 2, the numerical approaches are described, and a grid independence study and validation is reported. Reported results include a description of the incidence-angle-dependence of three-dimensional bifurcations in § 3.1, simulated dye visualizations in § 3.2, Floquet analysis results in § 3.3, three-dimensional wake structure in § 3.4, nonlinear modelling of three-dimensional bifurcations in § 3.5, wake pattern formation at higher Reynolds number in § 3.6, and Strouhal–Reynolds number dependencies in § 3.7. Far-wake fluctuations

https://doi.org/10.1017/S0022112009006879 Published online by Cambridge University Press

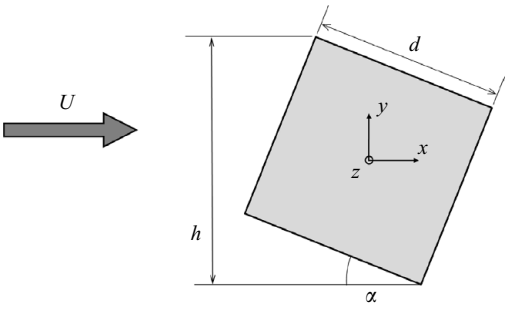


FIGURE 1. Schematic diagram of the system under investigation, showing cylinder side length d, projected frontal height h, free stream velocity U and the Cartesian coordinate system.

have been reported in previous studies (Sohankar *et al.* 1999). In the Appendix, the origin and control of this instability is investigated.

2. Methodology

The system under investigation in this paper comprises a cylinder with a square cross-section (side length d) inclined at an angle of incidence (α) to an oncoming free stream with velocity U. A schematic diagram of this system is shown in figure 1. The cylinder presents a height $h = d(\sin(\alpha) + \cos(\alpha))$ to the oncoming flow, which serves as a reference length for the dimensionless parameters in this investigation. A Reynolds number is defined as

$$Re = \frac{Uh}{\nu}, \tag{2.1}$$

where ν is the kinematic viscosity of the fluid. Wake shedding frequencies (f) are characterized by a Strouhal number, defined as

$$St = \frac{fh}{U}. \tag{2.2}$$

It is noted that Reynolds and Strouhal numbers based on the side length d can be recovered by dividing (2.1) and (2.2) by $\sin(\alpha) + \cos(\alpha)$.

2.1. *Numerical treatment*

The incompressible Navier–Stokes equations are solved using a spectral-element discretization in space (Karniadakis & Triantafyllou 1992) and a third-order backwards-multistep method in time (Karniadakis, Israeli & Orszag 1991; Blackburn & Sherwin 2004). The present code has been used and validated in Sheard *et al.* (2007) to investigate the flow past arresting cylinders, and facilitates two-dimensional computation on a mesh comprising of nodal quadrilateral spectral elements. Three-dimensional flows in spanwise-homogeneous geometries are computed by means of a spectral-element/Fourier algorithm (Karniadakis & Triantafyllou 1992; Thompson *et al.* 1996; Blackburn & Sherwin 2004), in which the flow variables are discretized in the spanwise direction using a Fourier series. This naturally imposes a periodic condition on the flow in the spanwise direction.

A stability analysis algorithm is employed to determine the stability of two-dimensional flow solutions to three-dimensional perturbations following Barkley & Henderson (1996). A periodic two-dimensional flow is evolved using the Navier–Stokes equations, and three-dimensional perturbation fields are computed using

https://doi.org/10.1017/S0022112009006879 Published online by Cambridge University Press

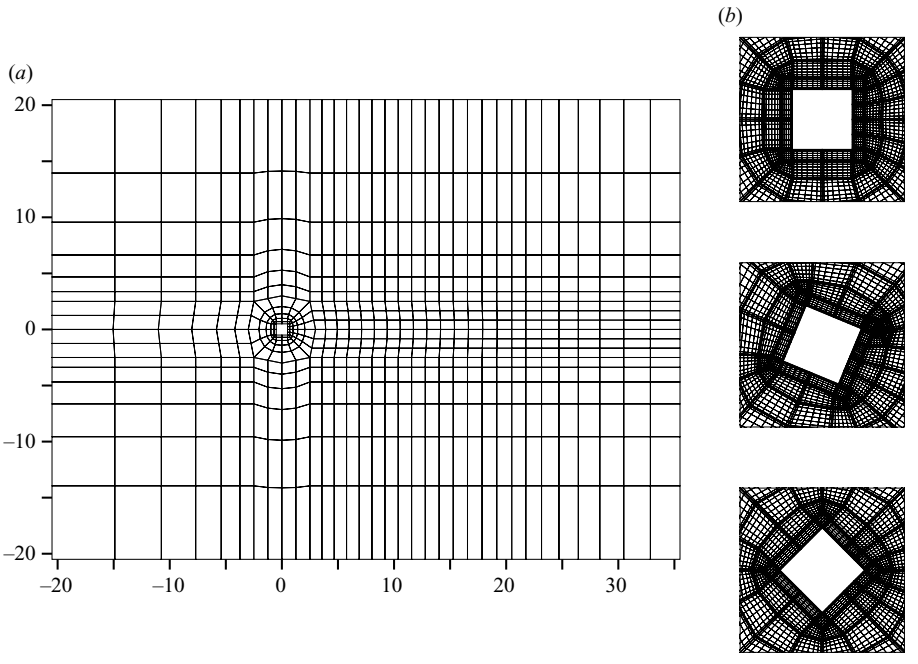


FIGURE 2. Examples of the meshes employed in this study. (*a*) The complete computational domain. (*b*) Mesh detail in the vicinity of cylinders with (top) $\alpha = 0°$, (middle) 22.5° and (bottom) 45° with interpolation grids within each element shown.

linearized Navier–Stokes equations. The perturbations vary sinusoidally in the spanwise direction, and each perturbation wavenumber (m) couples only with the two-dimensional base flow, and not other perturbations. This allows the stability of three-dimensional perturbations to be determined both as a function of Re and m. The stability analysis supplies eigenvalues and eigenvectors, corresponding to the Floquet multipliers (or amplification factors) of leading instability modes at a given wavenumber, and perturbation flow fields corresponding to the modes. Typically, only the leading eigenvalue is of interest as this relates to the fastest growing mode at a given Reynolds number and wavenumber. The Floquet multiplier is complex, and instability modes are classified as follows: regular modes have Floquet multipliers containing only a positive real component, subharmonic modes have only a negative real component and quasi-periodic modes arise from a complex-conjugate pair of multipliers with a non-zero imaginary component.

The leading eigenvalues and eigenvectors arising from the stability analysis are resolved in the present code using either a power method (as employed in Sheard & Ryan 2007), or an Arnoldi method (Barkley & Henderson 1996; Blackburn & Lopez 2003), which is implemented through the ARPACK package (Lehoucq, Sorenson & Yang 1998). To exploit efficiency through parallelization, eigenvalues were typically resolved using the power method with numerous spanwise wavenumbers being computed concurrent to a single base flow. However, the magnitude of quasi-periodic modes were confirmed by subsequent application of the implicitly restarted Arnoldi method.

Figure 2 shows the meshes employed in this study. At the left domain boundary, a unit velocity field is imposed to create a free stream flowing from left to right.

https://doi.org/10.1017/S0022112009006879 Published online by Cambridge University Press

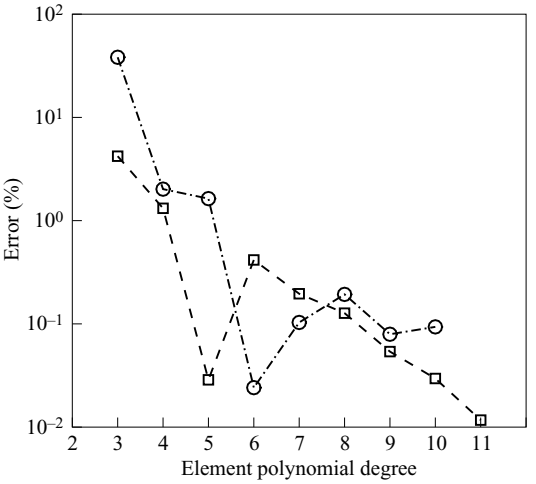


FIGURE 3. Percentage error in Strouhal number plotted against element polynomial degree at both $Re = 141$ and $\alpha = 45°$ (□), and $Re = 300$ and $\alpha = 0°$ (○). Dashed lines are included for guidance.

Along the top and bottom domain boundaries, stress-free impermeable boundaries were imposed in preference to a unit free stream velocity to minimize blockage effects. At the right domain boundary, a standard outflow boundary condition was imposed through a zero outward normal gradient of velocity and a constant reference pressure. A zero velocity (no-slip boundary) was imposed on the cylinder surface. To preserve the third-order time accuracy of the scheme, a suitable Neumann boundary condition was imposed on the outward normal gradient of pressure at boundaries where a Dirichlet condition was imposed on the velocity field, following Karniadakis, Israeli & Orszag (1991). All the meshes had approximately 644 elements, and 81 interpolation points per element featured throughout. The blockage ratio varies between 2.4 % and 3.4 % for incidence angles $\alpha = 0°$ to 45°. Sohankar *et al.* (1999) reported a reduction in the Strouhal number of 1.4 % as the blockage ratio was reduced from 5 % to 2.5 %. These correspond to the values used by Robichaux *et al.* (1999) and the present study, respectively. In the present study, the domain extended upstream by $20d$ and downstream by $35d$, which were found to be sufficiently large that domain errors were negligible. The significantly longer downstream distance, when compared with earlier studies, was used to capture features developing in the far wake.

2.2. *Grid independence and validation*

A grid independence study was performed to determine the variation in error with element polynomial degree. The Strouhal number was monitored (Thompson *et al.* 1996; Sheard 2007) in two cases ($Re = 141$, $\alpha = 45°$ and $Re = 300$, $\alpha = 0°$), and the error was taken as the per cent difference between the Strouhal number obtained at each resolution with a higher resolution reference case computed under the same conditions. The results are plotted in figure 3.

In both cases, errors of less than 0.1 % were obtained with polynomial degree 9, which was employed throughout the remainder of this study. The resulting meshes contain approximately 41×10^3 nodes. Solutions were stable in time and exhibited negligible time integration errors when a time step of $\Delta t = 0.0025d/U$ was used.

https://doi.org/10.1017/S0022112009006879 Published online by Cambridge University Press

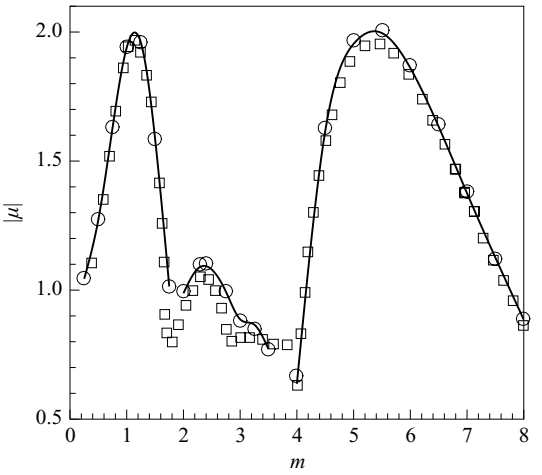


FIGURE 4. Floquet multiplier magnitudes ($|\mu|$) plotted against spanwise wavenumber (m) for a square cylinder at zero-incidence angle at $Re = 205$. The solid curves denote the present data, and the data from Robichaux *et al.* (1999) and Blackburn & Lopez (2003) are indicated by squares and circles, respectively.

In order to validate the stability analysis algorithm employed in this study, a comparison is made to the earlier results reported by Blackburn & Lopez (2003). Their calculations deliberately reproduced the small domain employed by Robichaux *et al.* (1999), who were the first to investigate the three-dimensional instabilities in the wake behind a square cylinder at zero-incidence angle. To achieve a reliable comparison with these earlier studies, a mesh was produced to the precise dimensions used in those studies (i.e. distances from the surface of the cylinder to the upstream, transverse and downstream boundaries of $5d$, $8.5d$ and $17d$, respectively), with identical element distributions and polynomial degree 16 being employed. In the present computation, a free stream velocity field was imposed on the upstream and transverse boundaries, and an outflow boundary comprising a zero normal gradient of velocity and a constant reference pressure was imposed. This again was consistent with Robichaux *et al.* (1999), with the exception of the outflow boundary, where they instead employed a buffer-domain technique (Mittal & Balachandar 1996). A two-dimensional flow solution was obtained at $Re = 205$, and the stability of this flow was determined over a range of spanwise wavenumbers $0.25 \leqslant m \leqslant 8$. Data from Robichaux *et al.* (1999) and Blackburn & Lopez (2003) was digitized, and is included in figure 4 along with the present results. The results of Blackburn & Lopez (2003) are reproduced with the present algorithm to a high fidelity, demonstrating the accuracy of the present technique.

3. Results

3.1. *Three-dimensional bifurcation scenario*

The three-dimensional stability of the wakes was determined by means of a linear stability analysis at seven equi-spaced incidence angles in the range $0° \leqslant \alpha \leqslant 45°$. The analysis provides growth rates of instability modes as a function of Re and the spanwise wavenumber m. Polynomial interpolation was employed to identify the Reynolds numbers at which the three-dimensional modes were neutrally stable (zero growth rate), and the results of this analysis are summarized in figure 5.

https://doi.org/10.1017/S0022112009006879 Published online by Cambridge University Press

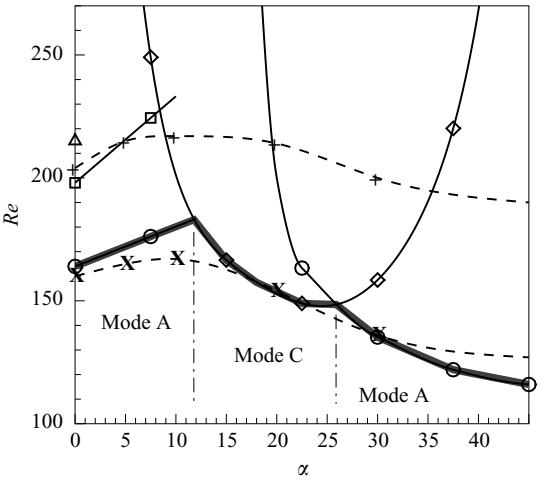


FIGURE 5. Predicted critical Reynolds numbers for three-dimensional instability modes plotted against incidence angle (α). For comparison, the experimental results of Tong *et al.* (2008) (dashed lines) are included, with modes A and B represented by '×' and '+', respectively. Solid lines are added to the current data for guidance, which includes modes A (○) and B (□), the subharmonic mode C instability (◇) and the quasi-periodic mode (△). A thick line traces the predicted threshold between two- and three-dimensional flow, and the first-occurring three-dimensional instability mode over ranges of incidence angle are labelled with these ranges separated by vertical dash-dotted lines.

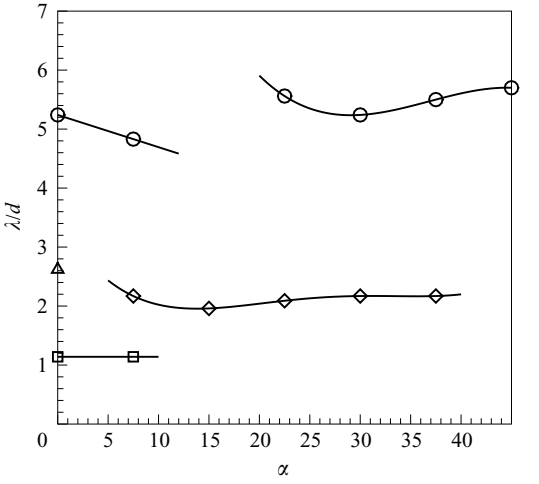


FIGURE 6. Spanwise wavelengths (λ/d) of three-dimensional modes at the onset of their instability, plotted against incidence angle (α). Solid lines are added to the current data for guidance, and symbols show mode A (○), mode B (□), mode C (◇) and the quasi-periodic mode (△).

The wavelengths at which the maximum growth rate was obtained for each mode was also determined from this analysis, and these results are plotted in figure 6.

In a recent experimental study, Tong *et al.* (2008) suggested that the wake behind a square cylinder transitioned to three-dimensional flow through the mode A instability, with a subsequent transition to mode B occurring for all incidence angles as the

https://doi.org/10.1017/S0022112009006879 Published online by Cambridge University Press

Reynolds number was increased. In that study, the transition Reynolds number to mode A was found to increase as the incidence angle increased from $\alpha = 0^\circ$ to 10°. Curiously, with further increases in incidence angle, the transition Reynolds number reversed this trend and began to decrease. A similar trend was also recorded for the mode B transition.

In Tong *et al.* (2008), three-dimensional transition was identified using hotwire anemometry. Following Williamson (1988*b*), the first and second discontinuities in the Strouhal–Reynolds number profiles were taken to represent the transitions to modes A and B, respectively. Visualization was conducted using the method of dye injection, whereby dye was injected into the flow from the top face of the cylinder to reveal the three-dimensional structure of the vortices shed into the wake. Visualizations were presented at $\alpha = 0^\circ$, 10° and 45° with measurements of the spanwise wavelengths of the first-occurring three-dimensional wake structures being in the range of $4d$–$5d$, which is consistent with the mode A instability (Blackburn & Lopez 2003).

The present stability analysis reveals that the first-occurring three-dimensional instability mode actually depends on the incidence angle. At small incidence angles, three-dimensional flow is predicted to develop through a mode A instability. However, as α increases, mode A is predicted to weaken. From 0° to 7.5°, growth rates over the mode A waveband were found to reach a local maximum with increasing Reynolds number, before subsequently decreasing, and this peak growth rate decreased with increasing incidence angle. Presumably, the distortion of the two-dimensional wake with changing incidence angle acts to suppress the mode A instability. Interpolation between data acquired at 7.5° and 15° yielded a critical incidence angle $\alpha \approx 12$, above which mode A is not predicted to arise, as growth rates in the mode A waveband remain negative (two-dimensionally stable).

At all non-symmetrical incidence angles tested (7.5°–37.5°), growth rates corresponding to a subharmonic instability mode occurring with a spanwise wavenumber of $m \approx 3$ were detected. It will be shown that this mode is consistent with the mode C instability discovered in the wakes behind rings by Sheard *et al.* (2003), and also observed behind offset tandem cylinders by Carmo *et al.* (2008). The mode C instability becomes more unstable as α increased from 0°, and becomes the first-occurring instability beyond 12°.

The trend towards a wake with centreline symmetry as $\alpha \to 45^\circ$ was found to suppress the mode C instability, and promote the mode A instability. At 22.5°, positive growth rates were again predicted in the mode A waveband, though at this incidence angle the mode C instability is predicted to be the first-occurring mode. Beyond $\alpha \approx 26^\circ$, this behaviour is reversed, and mode A resumes as the first-occurring three-dimensional instability mode. As expected, no evidence of the mode C instability was detected at $\alpha = 45^\circ$.

In summary, three-dimensional flow develops through three distinct bifurcations, depending on incidence angle: a small-incidence-angle mode A branch below 12°, a mode C branch between 12° and 26° and a large-incidence-angle mode A branch above 26°. The characterization of the appearance of the mode A instability as two distinct branches is supported by the incidence-angle variation of the predicted spanwise wavelengths of the mode A instability in figure 6. The small-incidence-angle branch displays a decrease in the spanwise wavelength from $5.2d$ to $4.8d$, whereas the re-emergence of the mode A instability beyond $\alpha \approx 20^\circ$ occurs with a wavelength decreasing from approximately $5.8d$: the two trends are clearly not part of a continuous profile.

https://doi.org/10.1017/S0022112009006879 Published online by Cambridge University Press

Autocorrelation measurements reported in Tong *et al.* (2008) showed that the mode A instability had a longer spanwise wavelength at 10° than at 0°, contrary to the present prediction. It should be noted, though, that the wavelengths reported in figure 6 represent three-dimensional modes at the onset of their transition. The fastest growing modes were generally found to vary with Reynolds number, so that there could well be a difference between the wavelength in the immediate vicinity of the transition Reynolds number, and at the higher Reynolds numbers at which the experimental measurements were performed. Moreover, beyond the onset of the transition, a finite band of wavelengths are unstable, allowing experimental conditions (end effects, aspect ratio, etc.) to influence the prevailing spanwise wavelength of a three-dimensional mode. For example, our analysis predicts that at $Re = 172$ and $\alpha = 7.5°$ the mode A instability is unstable over wavelengths $3.9d \lesssim \lambda \lesssim 7.9d$.

Figure 5 provides an explanation for the local peak in three-dimensional transition Reynolds number measured by Tong *et al.* (2008) at $\alpha \approx 10°$. The present analysis reveals that the peak occurs at a cross-over between the small-incidence-angle mode A branch and the mode C branch, rather than being a local peak in a single mode A transition Reynolds number profile.

The present bifurcation scenario also explains why the dye visualizations of Tong *et al.* (2008) (see their figure 5) only displayed evidence of mode A and mode B instability modes, and not the mode C instability predicted here: Mode A is predicted to be the first-occurring instability at each of the incidence angles they presented (0°, 10° and 45°). Few intermediate-wavelength three-dimensional instability modes have been visualized experimentally (e.g. see Zhang *et al.* 1995; Sheard *et al.* 2005), and no visualizations of such modes in the square cylinder wake in the three-dimensional transition regime are known to the authors.

3.2. *Simulated dye visualizations: mode A or mode C?*

Three-dimensional direct numerical simulations were conducted in conjunction with simulated particle tracking (Sheard *et al.* 2007) to investigate the likely structure of the wake at incidence angles in the mode C regime. Simulations were performed at 0° for direct comparison with the dye visualizations of Tong *et al.* (2008), and at 15° to elucidate the appearance of the wake structure through evolution of three-dimensional flow in the wake in the mode C incidence angle range. At $\alpha = 0°$, the wake was computed at $Re = 188$ and 244, and the results are plotted in figure 7. The simulations were performed with a spanwise wavelength equal to the wavelength of the mode A instability at each incidence angle, and several spanwise periods of the solutions are displayed for comparison purposes. Based on the predicted spanwise wavelengths of the mode C instability shown in figure 6, a mode C instability would be identified by a three-dimensional pattern in the wake with a wavelength of approximately $2d$. In both the experiments and the simulations, the visualization medium is injected from the top of the cylinder. This comparison demonstrates that dye structures at $Re = 188$ in the experiments are indeed consistent with the development of the mode A instability, and at $Re = 244$ the smaller scale structures associated with the mode B instability are visible in both the experimental and numerical frames.

The simulations at 15° are shown in figure 8, and it can be seen that the dominant spanwise structure has a spanwise wavelength of approximately $2.6d$, which is consistent with the mode C instability. It is currently unknown whether these simulated visualizations can be (or indeed have been) observed experimentally: this would be a useful direction for future work.

https://doi.org/10.1017/S0022112009006879 Published online by Cambridge University Press

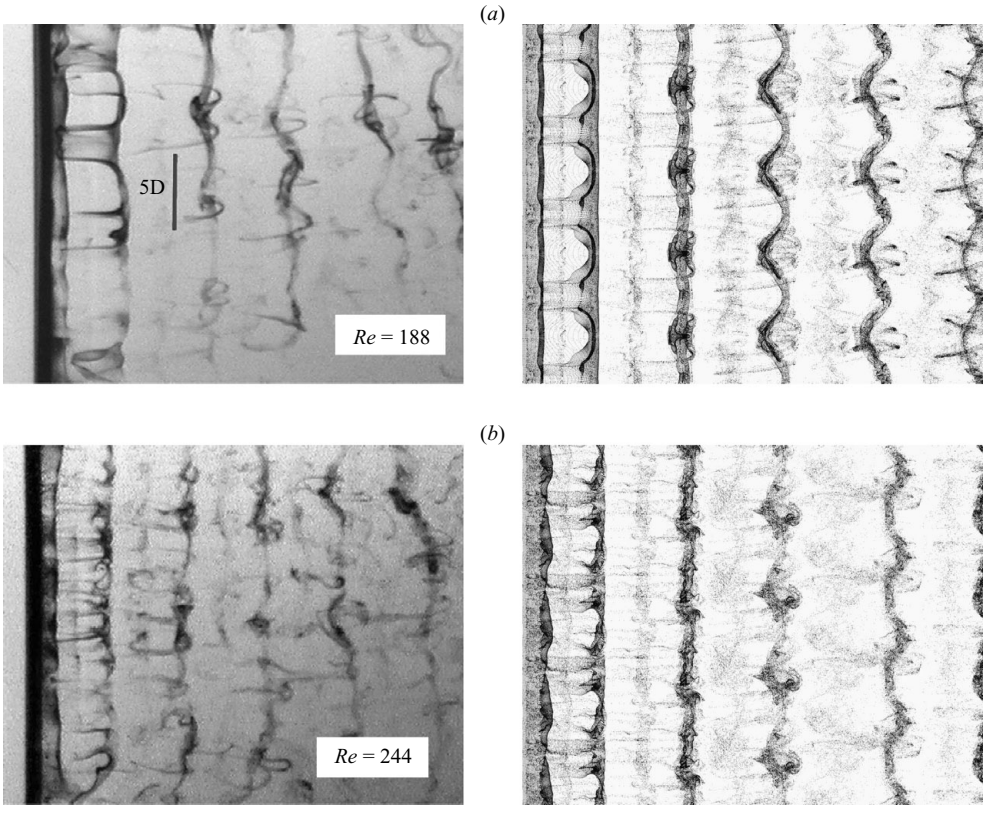


FIGURE 7. A comparison between experimental dye visualization (left, reproduced with permission from Tong *et al.* 2008) and three-dimensional numerical simulations injected with passive tracer particles (right). Wakes are shown with $\alpha = 0°$ and $Re = 188$ (a) and 244 (b). Flow is from left to right, the cylinder is at the left of each frame and dye/particles are injected from the upper surface of the cylinder.

3.3. *Wavenumber dependence of Floquet multipliers at* $\alpha = 0°$, $22.5°$ *and* $45°$

The stability of the wakes at three incidence angles will now be studied in detail to underpin the bifurcation scenario painted in figure 5. Plots of Floquet multiplier against wavenumber at incidence angles 0°, 22.5° and 45° are shown in figures 9–11, respectively.

Figure 9 shows the results at $\alpha = 0°$. Floquet multipliers were computed at a range of Reynolds numbers and spanwise wavelengths to identify the neutral stability thresholds ($|\mu| = 1$) of any available instability modes in the wake. The previous stability analyses of a square cylinder at zero angle of incidence (Robichaux *et al.* 1999; Blackburn & Lopez 2003) were performed on a significantly smaller domain than those employed in the present study. If the data at $Re = 205$ in figure 9 is compared with the validation data in figure 4, it can be seen that smaller Floquet multipliers are predicted from stability analyses computed on the larger domain. This effect is most pronounced at the peak of the high-wavenumber mode, which achieves a maximum of $|\mu| = 1.46$ at $m \approx 5.4$ in figure 9. From the calculations on the smaller domain, an artificially amplified peak of $|\mu| = 2.0$ is predicted, occurring at the same wavenumber. The present computational domain is larger in every direction (inflow, transverse and outflow) than the domain used in the validation study, vastly reducing

https://doi.org/10.1017/S0022112009006879 Published online by Cambridge University Press

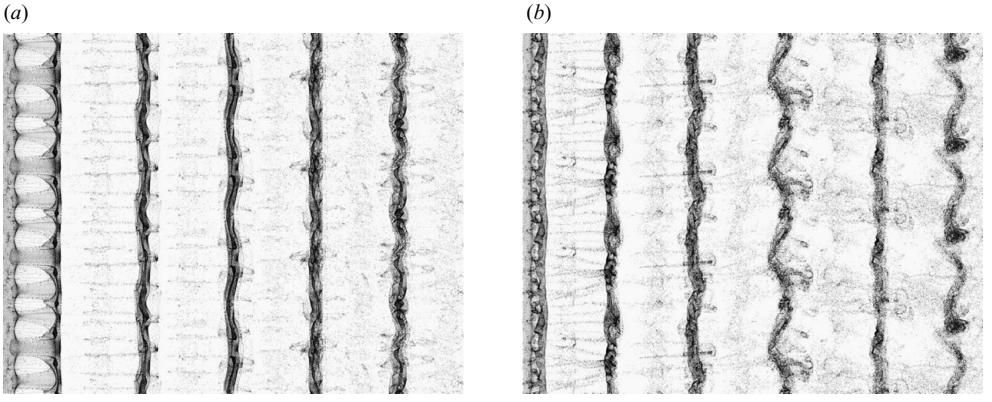


FIGURE 8. Simulated dye visualization computations of the wake at $\alpha = 15°$ at $Re = 188$ (*a*) and 244 (*b*). Field of view is as per figure 7.

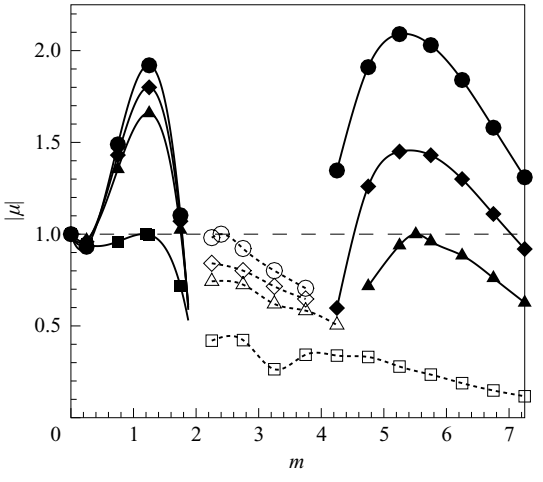


FIGURE 9. Floquet multiplier magnitude $|\mu|$ plotted against spanwise wavenumber m for a square cylinder at $\alpha = 0°$ (the wavenumber relates to the spanwise wavelength by $\lambda = 2\pi d/m$). Reynolds numbers (□) $Re = 164$, (△) 197, (◇) 205 and (○) 215 are plotted. Filled black symbols and solid curves show real Floquet multipliers (synchronous modes); hollow symbols and dotted curves correspond to complex-conjugate Floquet multipliers (quasi-periodic modes). Curves are included for guidance, and the neutral stability threshold at $|\mu| = 1$ is also shown by a dashed line.

the domain effects on the flow, and therefore reducing the contamination of Floquet multiplier predictions due to the domain size.

To contextualize this finding in relation to earlier stability analysis studies, Barkley & Henderson (1996) reported that Floquet multipliers did not alter significantly when the stability analysis was performed on smaller computational domains. However, in that study, the smallest domain used was larger than that employed by Robichaux *et al.* (1999) (upstream length $8d$ versus $5.5d$, transverse length $8d$ versus $8.5d$ and downstream length $25d$ versus $17.5d$), thus avoiding the most extreme influence of the domain on the predicted Floquet multipliers. Moreover, the base flow employed in their stability analyses on smaller meshes was interpolated from their largest mesh, and thus the perturbation was permitted to evolve on a base flow which was not adversely affected by the smaller domain sizes. In light of this, the present predictions

https://doi.org/10.1017/S0022112009006879 Published online by Cambridge University Press

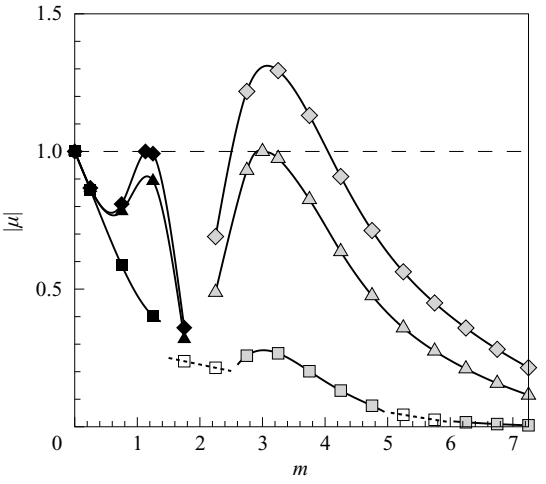


FIGURE 10. Floquet multiplier magnitude $|\mu|$ plotted against spanwise wavenumber m for a square cylinder at $\alpha = 22.5°$. Reynolds numbers (□) $Re = 98$, (△) 149 and (◇) 163 are plotted. Grey shaded symbols and solid curves correspond to negative real Floquet multipliers (subharmonic modes); real and complex modes are identified as per figure 9.

of the critical Reynolds numbers for the onset of three-dimensional flow improve on the values predicted by Robichaux *et al.* (1999).

In the present computations shown in figure 9, peaks consistent with mode A and B instabilities are predicted to become neutrally stable at $Re = 164$ and $Re = 197$, respectively, and a quasi-periodic mode is predicted to become unstable at $Re \approx 215$. These modes are most unstable at spanwise wavenumbers $m = 1.2$, 5.5 and approximately 2.4, respectively ($\lambda/d = 5.2$, 1.1 and 2.6, respectively). Up to $Re \approx 210$, mode A is the fastest growing instability mode.

The results of the $\alpha = 22.5°$ case are shown in figure 10. Two distinct real modes are predicted. The wake is firstly unstable to a mode with spanwise wavenumber $m = 3.0$ ($\lambda/d = 2.1$) at $Re = 149$. At $Re = 163$ a second mode crosses the neutral stability threshold with a spanwise wavenumber of $m = 1.1$ ($\lambda/d = 5.6$). It will be shown that these modes were consistent with mode C and mode A instabilities, respectively. Quasi-periodic Floquet modes were also detected over a narrow band of spanwise wavelengths at lower Reynolds numbers, though these did not become unstable over the range of Reynolds numbers investigated ($Re \leqslant 163$).

Figure 11 shows the stability of the cylinder wake at $\alpha = 45°$. The wake was found to be unstable to an instability with $m = 1.1$ ($\lambda/d = 5.7$) beyond $Re = 116$, which will be shown to be consistent with a mode A instability. Wake stability was not investigated beyond $Re \approx 140$ as the two-dimensional base flow became aperiodic. This aperiodicity developed as a result of the vortices in the wake separating into two parallel rows. No additional instability modes were detected at these Reynolds numbers.

3.4. *Mode symmetry and structure*

Comparisons are now presented between the predicted three-dimensional instability modes identified in the previous section, and the corresponding three-dimensional wakes computed by means of direct numerical simulations. Three-dimensional isosurface plots have been generated by superimposing the Fourier mode of the instability onto the two-dimensional base flow. In addition, three-dimensional

https://doi.org/10.1017/S0022112009006879 Published online by Cambridge University Press

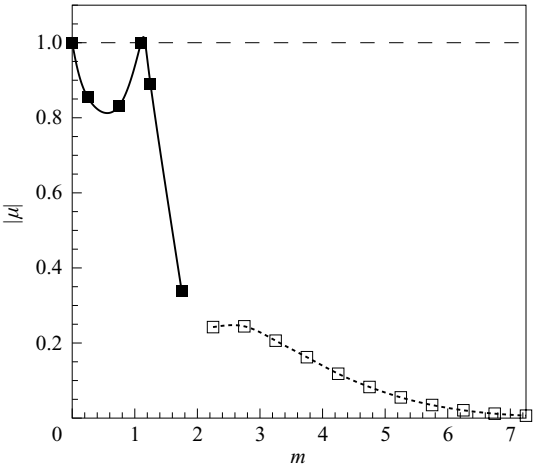


FIGURE 11. Floquet multiplier magnitude $|\mu|$ plotted against spanwise wavenumber m for a square cylinder at $\alpha = 45°$ and $Re = 116$. Real and complex modes are identified as per figure 9.

simulations with the same spanwise wavelengths have been performed at Reynolds numbers slightly above the predicted critical Reynolds numbers for each of the transition modes. The spanwise wavelength of each three-dimensional simulation is represented by the wavenumbers (m) given in captions for figures 12–14. The spectral-element/Fourier computations employed 15 spanwise Fourier modes, which was found by tests to be sufficient to resolve the three-dimensional wake structures. These plots reveal details about the spatio-temporal symmetry and vortical structure of the modes. For clarity, the spanwise phase of the three-dimensional wakes have been shifted to match the stability analysis results.

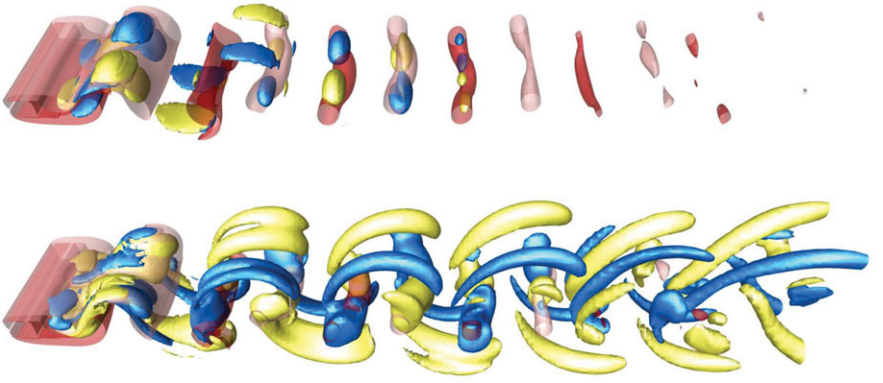
The plots in figure 12 show the modes computed at $\alpha = 0°$. In figure 12(a), the spatio-temporal symmetry of both the perturbation field and the three-dimensional simulation are the same. Evolving the wake by one half-period and reflecting about the centreline (a *half-period flip*) produces an identical flow. This is characteristic of the mode A instability (Barkley & Henderson 1996). It is notable that the visible isosurfaces of streamwise vorticity extend much further downstream in the three-dimensional wake than in the perturbation field, signifying the substantial modification of the wake through the nonlinear growth regime of the instability.

Figure 12(b) shows wakes consistent with the mode B instability, which has a spatio-temporal symmetry whereby a half-period flip and a spanwise translation of half a wavelength of the mode ($\lambda/2$) recovers the original flow. In terms of the streamwise vorticity field, this symmetry dictates that the sign of vorticity at a point in the wake is equal to the sign of vorticity at a point reflected about the wake centreline and shifted one half period in time. In the three-dimensional simulation the mode B wake structures diffuse within 3–4 shedding cycles, and the Floquet mode structure can clearly be seen in the saturated wake.

In figure 12(c) the quasi-periodic mode is plotted alongside the corresponding three-dimensional wake. As the Reynolds number for this simulation was higher than that of the mode B wake shown in figure 12(b), and the spanwise extent of the computational domain was longer, the mode B instability was free to evolve in competition with the quasi-periodic mode. In approximately the first two-thirds of the visible three-dimensional wake, three-dimensional structures resembling the mode

https://doi.org/10.1017/S0022112009006879 Published online by Cambridge University Press

(*a*) $m = 1.2$, (top) $Re = 164$ and (bottom) $Re = 180$.



(*b*) $m = 5.5$, (top) $Re = 196$ and (bottom) $Re = 210$.



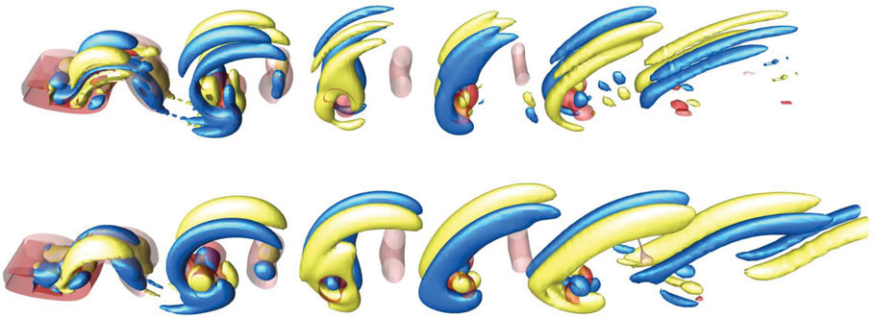
(*c*) $m = 2.4$, (top) $Re = 213$ and (bottom) $Re = 230$.



FIGURE 12. Three-dimensional isosurface plots of the wakes behind a square cylinder at an angle of incidence $\alpha = 0°$. Each pair is drawn to the same scale, with the top image showing the leading eigenvector fields of the instability modes at the predicted onset of the instability superimposed onto the base flow, and the bottom images showing the corresponding saturated three-dimensional wakes computed using the spectral-element/Fourier algorithm at Reynolds numbers above the predicted onset of the instability. Flow is left to right, and the images are shown at the instant of peak lift force. Translucent isosurfaces show spanwise vorticity ($\omega_z d/U = \pm 1$), and three-dimensionality is revealed by opaque light and dark isosurfaces of streamwise vorticity ($\omega_x d/U = \pm 0.2$).

https://doi.org/10.1017/S0022112009006879 Published online by Cambridge University Press

(*a*) $m = 3.0$, (top) $Re = 146$ and (bottom) $Re = 170$.



(*b*) $m = 1.13$, (top) $Re = 173$ and (bottom) $Re = 183$.

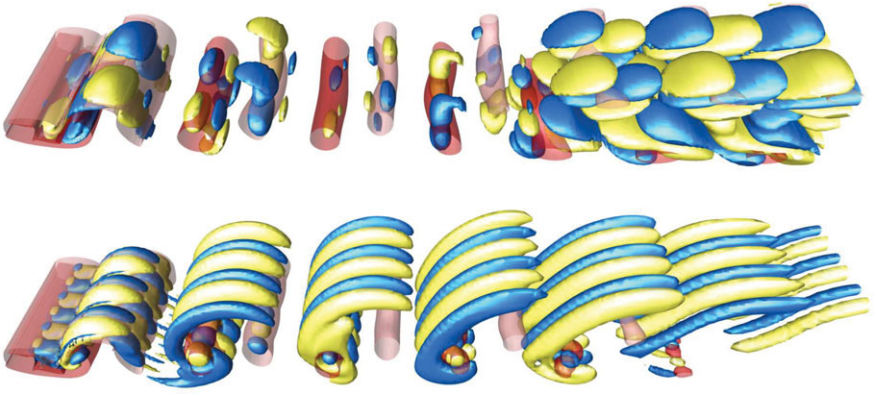


FIGURE 13. Three-dimensional isosurface plots of the wakes behind a square cylinder at an angle of incidence $\alpha = 22.5°$. Contours and shading are as per figure 12. In (*b*) the three-dimensional wake exhibits mode C wake structures in preference to the predicted mode A instability.

B wake are observed. Close inspection of the sign of successive streamwise vortices along the span reveals that here two spanwise periods of the mode B instability have emerged in preference to a wake resembling the quasi-periodic mode. Further downstream, three-dimensional structures with a wavelength matching the span of the computational domain are visible, though it is apparent that the wake is dominated by three-dimensional structures consistent with the mode B instability. This behaviour is consistent with the circular cylinder, where in fact mode B has been observed to persist to very high Reynolds numbers (Mansy *et al.* 1994; Wu *et al.* 1996), despite stability analysis predicting a quasi-periodic mode becoming unstable beyond the onset of mode B. However, it must be noted that stability analysis predictions beyond the first-occurring transition must be treated with caution as the true three-dimensional flow is no longer consistent with the original two-dimensional solution.

In figure 13 the wakes at $\alpha = 22.5°$ are plotted. In figure 13(*a*), the stability analysis and three-dimensional simulations both display a mode consistent with a subharmonic mode C instability (Sheard *et al.* 2005). Due to the lack of a reflective symmetry of the geometry or the time-averaged wake in this case, this mode adopts a $2T$-periodic symmetry: i.e. the wake has undergone a period doubling as a result of

https://doi.org/10.1017/S0022112009006879 Published online by Cambridge University Press

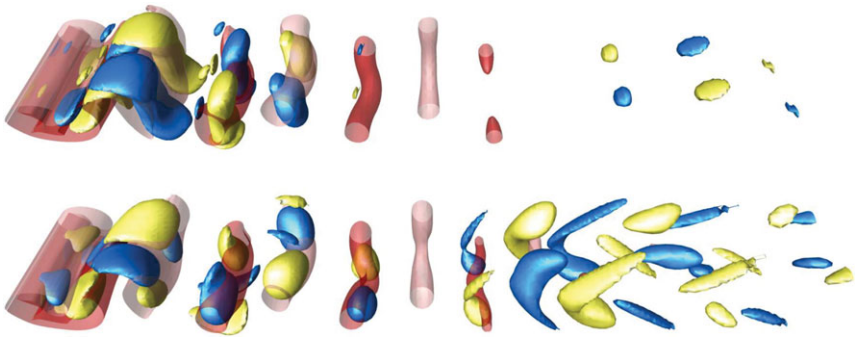


FIGURE 14. Three-dimensional isosurface plots of the wakes behind a square cylinder at an angle of incidence $\alpha = 45°$. The spanwise wavenumber is $m = 1.1$ and the solutions were computed at (top) $Re = 116$ and (bottom) $Re = 127$. Contours and shading are as per figure 12.

the instability mode developing with a negative real Floquet multiplier. The structure of the perturbation field and the three-dimensional wake are very similar, with strong bands of streamwise vorticity arcing over pairs of shed vorticies. Curiously, these vorticity bands are absent from the underside of the wake.

Interestingly, figure 13(*b*) demonstrates that while a wake consistent with a mode A instability is predicted as a second three-dimensional instability at this angle of incidence, the corresponding three-dimensional simulation shows that a wake consistent with the mode C instability persists in preference to the mode A instability. Here the perturbation field exhibits strong structures in the far wake, which are not typically observed in stability analyses of cylinder wakes due to the longer downstream domain employed here. The three-dimensional wake shows three spanwise periods of the mode C wake structures in preference to structures consistent with a mode A instability.

Plots of the wakes corresponding to the instability predicted with $\alpha = 45°$ are shown in figure 14. This mode displays a spatio-temporal symmetry consistent with a mode A instability, and a close similarity is observed between the perturbation field and the three-dimensional wake.

The appearance of the shorter wavelength instability in the three-dimensional computations at $\alpha = 0°$ (mode B observed beyond the predicted onset of the quasi-periodic mode), and at $\alpha = 22.5°$ (mode C observed beyond the predicted onset of mode A) follows the trends in growth rates of the respective instability modes (see figures 9 and 10, respectively). Figure 9 shows that at onset of the quasi-periodic mode, the shorter-wavelength mode B instability has a substantially higher growth rate. Similarly, figure 10 demonstrates that at onset of mode A, the mode C instability also has a higher growth rate.

3.5. *Three-dimensional wake transition: nonlinear dynamics*

Linear stability analysis can inform on the spanwise wavelength, critical Reynolds number and spatiotemporal symmetry of a predicted three-dimensional transition, but it cannot provide insight into nonlinear aspects of the transition. As a three-dimensional mode evolves on an unstable flow, its growth rate will change as a function of amplitude of the three-dimensional mode, before eventually approaching zero as the three-dimensional mode reaches a saturated state. This variation in growth rate and saturation is a result of nonlinear contributions to the solution. Several studies have modelled the evolution of a three-dimensional mode as a dynamical

https://doi.org/10.1017/S0022112009006879 Published online by Cambridge University Press

oscillator described by the Landau equation, including Henderson & Barkley (1996); Henderson (1997) for the mode A and B transitions behind a circular cylinder, Thompson, Leweke & Provansal (2001*a*) and Sheard, Thompson & Hourigan (2004) for the non-axisymmetric transitions behind a sphere and ring, respectively, and Carmo *et al.* (2008) for wake transitions behind staggered circular cylinders.

Those references should be consulted for details about the Landau equation and its application to characterizing the nonlinear dynamics of a three-dimensional wake transition. A brief overview is included here. The equation proposed by Landau & Lifshitz (1976) is

$$\frac{\mathrm{d}A}{\mathrm{d}t} = (\sigma + \mathrm{i}\omega)\, A - l\,(1 + \mathrm{i}c)\,|A|^2\, A + \cdots,$$

where $A(t)$ is a complex representation of the amplitude of the mode. The right-hand side comprises a series expansion of odd-numbered powers of A, with the first term describing the linear growth (growth rate σ and angular frequency ω) when A is very small, and higher terms being required to describe the nonlinear evolution and saturation of the mode. Manipulation of this equation provides two general behaviours depending on the sign of l. If l is positive, the mode will experience a decrease in growth rate towards zero as the amplitude increases. In this case, higher terms in the expansion are not required to describe the saturation of the mode, and it can be shown that a truncation of this equation at the cubic term permits only one amplitude at a given growth rate. This is consistent with a supercritical (or soft) bifurcation, for which the flow is stable for all Re below the transition, and unstable above it. Alternatively, if l is negative, higher terms in the expansion are required to describe the mode saturation, and this is consistent with a subcritical (or hard) bifurcation. Subcritical bifurcations permit a region of bistability in the vicinity of the transition: i.e. if the amplitude is small, the mode decays towards the two-dimensional solution branch, but at larger amplitudes, the three-dimensional mode grows and saturates. This provides an hysteretic behaviour in the vicinity of a subcritical bifurcation.

The nonlinear characteristics of the first-occurring three-dimensional transitions behind an inclined square cylinder at angles 0°, 22.5° and 45° were examined. These angles were chosen to capture each of the regimes of the onset of three-dimensional flow. The mode amplitude was measured from the envelope of the oscillation of the spanwise velocity component at a point in the wake. At 0° and 22.5°, the transition was found to arise through a supercritical bifurcation, yielding a positive l-coefficient. This suggests that the transition should be observed very close to the predicted transition Reynolds numbers from the linear stability analysis reported in this paper. At 45°, the transition was found to arise through a subcritical bifurcation, yielding a negative l-coefficient. Earlier analyses have shown mode A bifurcations behind a circular cylinder (Henderson & Barkley 1996) and rings (Sheard *et al.* 2004) consistently occur through a subcritical bifurcation. The present study demonstrates that this behaviour is not universal due to mode A occurring through a supercritical bifurcation at $\alpha = 0°$.

3.6. *Wake patterns and mode energy with a longer spanwise domain*

While the appearance of unique three-dimensional instability modes at Reynolds numbers in the vicinity of the transitions is of fundamental interest in an engineering context, the composition of the wake at higher Reynolds numbers is important. In order to address this, three-dimensional computations were performed at each incidence angle at $Re = 300$ and a computational domain with spanwise wavelength

https://doi.org/10.1017/S0022112009006879 Published online by Cambridge University Press

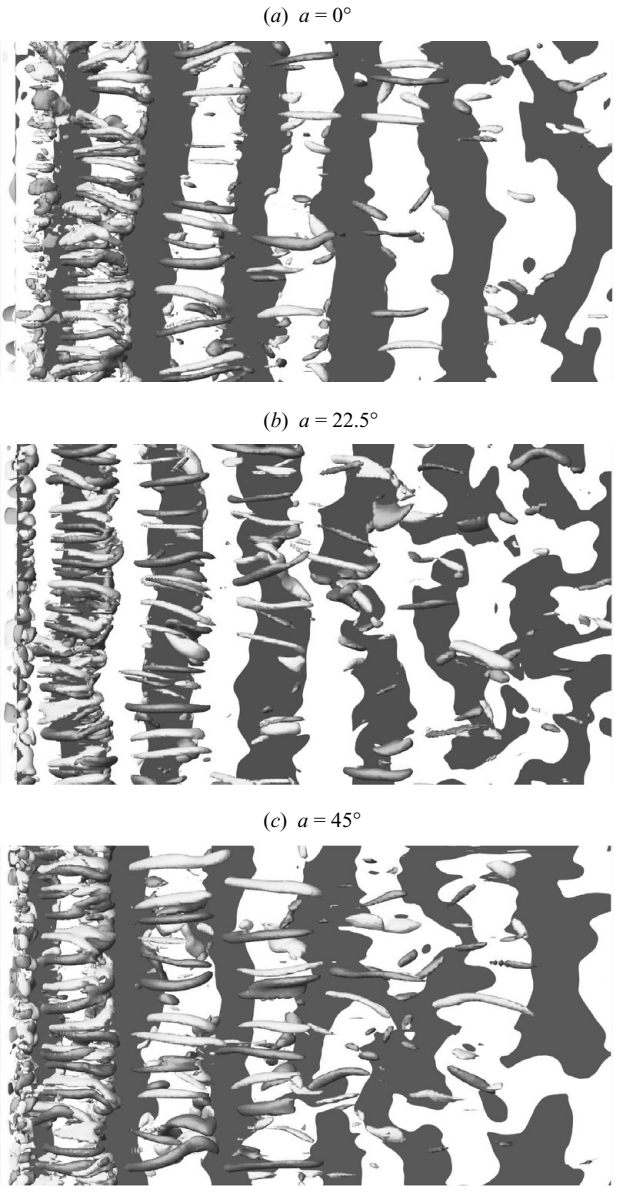


FIGURE 15. Plots showing the three-dimensional structure of the wakes behind a square cylinder at $Re = 300$ with a spanwise computational domain of $20d$. The vortex street is identified by contours of (white) positive and (black) negative out-of-plane velocity plotted on the $y = 0$ plane. Isosurfaces of streamwise vorticity with levels $\pm 1U/d$ are shaded light and dark. Flow is from left to right and, the cylinder (not shown) is located at the left of each frame.

$20d$. This Reynolds number is well beyond the onset Reynolds numbers for the three-dimensional instability modes predicted in this study, and the spanwise domain length is sufficient to permit several spanwise repetitions of the available three-dimensional modes to arise in the simulations. Isosurface plots exhibiting the three-dimensional structure of these wakes are provided in figure 15. Comparing these plots with the

https://doi.org/10.1017/S0022112009006879 Published online by Cambridge University Press

wakes shown in figures 12–14 demonstrates that at higher Reynolds numbers, and with a spanwise domain size large enough to include all the instability modes, the wakes exhibit a reduced structural uniformity. In the near wake, short-wavelength streamwise vortical structures are present, which have a spanwise wavelength consistent with the mode B instability. These streamwise vortical structures dissipate within 3 to 4 shedding cycles, beyond which the Kármán vortices distort and break up. The downstream wake is dominated by these dislocated spanwise vortices, and resembles the wake patterns identified as defect chaos by Leweke & Provansal (1995) (e.g. see their figure 31*a*) in their Ginzburg–Landau modelling of the vortex shedding behind rings, and as 'spot-like' disturbances in Henderson (1997) (e.g. see their figure 19). These patterns are examples of spatio-temporal chaos, where irregularity is present both in a spatially extended dimension (the spanwise direction) and in time. It is also noted that the irregular downstream wake patterns shown here also compare favourably with the experimental dye visualizations reproduced in figure 7. As discussed by Williamson (1992), one mechanism for the development of vortex dislocations involves the distortion of vortex rollers caused by the localized development of three-dimensional modes, leading to a spatial variation in phase across the wake.

These wake visualizations show that the relatively short-wavelength three-dimensional instability modes (i.e. A, B, C, etc.) which develop on the parallel vortex rollers of the near wake are replaced further downstream by the irregular patterns associated with spatio-temporal chaos. However, this presents a question: are the coherent three-dimensional mode structures disrupted and suppressed by deformations and dislocations of the vortex rollers, or do they provide a perturbation leading to an instability causing the breakdown to spatio-temporal chaos? It appears, based on the ability of the Ginzburg–Landau model (Shraiman *et al.* 1992; Leweke & Provansal 1994) to describe a similar spatio-temporally chaotic state in the absence of any perturbation analogous to those provided by secondary wake instabilities, that the correct interpretation is that spatio-temporal chaos naturally develops in the wake, and this subsequently suppresses the uniform structures associated with the evolution of instabilities such as mode A or B.

To further investigate the presence of spanwise structures in the wake, a quantitative description of the self-similarity of the solutions in the spanwise direction was ascertained by means of an autocorrelation analysis and a spanwise Fourier analysis of the solution.

At a number of locations along the wake centreline ($y = 0$) extending from directly behind the cylinder to $35d$ downstream, a one-dimensional autocorrelation of the spanwise variation of the velocity field was calculated. These autocorrelations were normalized by the variance of the signal, meaning that the autocorrelation function returned values ranging from 1, through 0, to -1, which corresponded to completely correlated, uncorrelated and inversely correlated signals, respectively. To achieve a global picture of the wake structures, the individual autocorrelation functions were averaged. If the wake possesses spanwise-periodic global structures with a shorter wavelength than the spanwise domain, these should appear as peaks in the autocorrelation function at a shift equal to their wavelength. Figure 16 shows the resulting mean autocorrelation functions for the three incidence angles considered. The unit correlation at spanwise shifts of 0 and $20d$ results from the spanwise periodicity over $20d$ imposed by the boundary conditions of the simulation. By taking the mean of a number of discrete autocorrelation functions, peaks corresponding to localized wake features have been obscured: indeed local peaks in some of the

https://doi.org/10.1017/S0022112009006879 Published online by Cambridge University Press

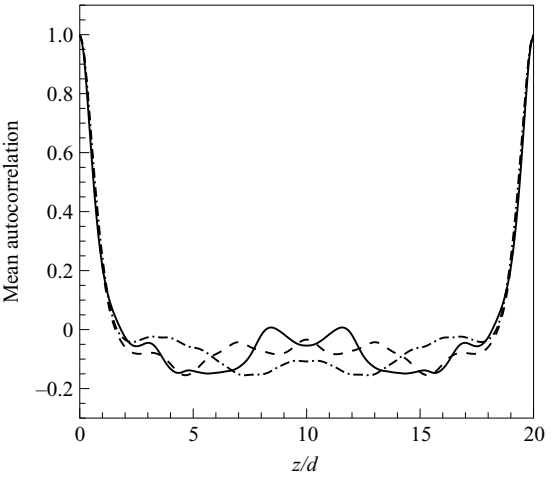


FIGURE 16. The mean of the spanwise autocorrelation functions for the z component of velocity sampled along the wake centreline. The wakes were computed at $Re = 300$. Angles of incidence $\alpha = 0°$ (solid curve), 22.5° (dashed curve) and 45° (dash-dotted curve) are shown.

autocorrelation functions suggested the presence of spanwise-repeating structures with wavelengths corresponding to each of the underlying three-dimensional instability modes reported in this study. However, there was no discernable evidence of any incidence-angle dependence of a particular mode over the others, and the mean autocorrelation functions demonstrate that these were isolated occurrences, and were not representative of the global spatial structure of the wake.

The determination that the dominant spanwise scale in the wake in these simulations is equal to the longest computed wavelength is further evidenced by the spanwise mode energy spectrum. The total kinetic energy in each spanwise Fourier mode was integrated over the computational domain, and to overcome the high spatio-temporal irregularity of these flows, a time-average of the mode energy spectrum was calculated from approximately 300 samples obtained over approximately 10 shedding cycles. While a greater number of samples would be desirable, the cost of these computations was prohibitive. The calculated time-averaged mode energy spectra are plotted in figure 17. The three curves demonstrate that the lowest wavenumbers contain the highest energy, and viscous diffusion compels a decrease in mode energy with an increase in wavenumber. No discernable peaks are seen at any of the plotted incidence angles at wavenumbers corresponding to modes A, B or C (i.e. $m \approx 1.2$, 6 or 3, respectively). This supports the conclusions drawn based on the autocorrelations shown in figure 16, regarding the spanwise wavelength of the dominant three-dimensional wake structures.

Of the three incidence angles shown in figure 17, the wake obtained at $\alpha = 0°$ displays the lowest mode energy at low wavenumbers, and the slowest decay of mode energy with increasing wavenumber. This reflects the structure of the flow visualized in figure 15, where the underlying vortex rollers are seen to remain parallel to a greater distance downstream with $\alpha = 0°$ than 22.5° or 45° before yielding to the development of spatio-temporal chaos. Hence there is less energy contained in small non-zero wavenumbers (the logarithmic scaling eliminates the $m = 0$ mode energy). It is speculated, therefore, that the development of spatio-temporal chaos may exhibit some incidence-angle dependence, with higher incidence angles developing

https://doi.org/10.1017/S0022112009006879 Published online by Cambridge University Press

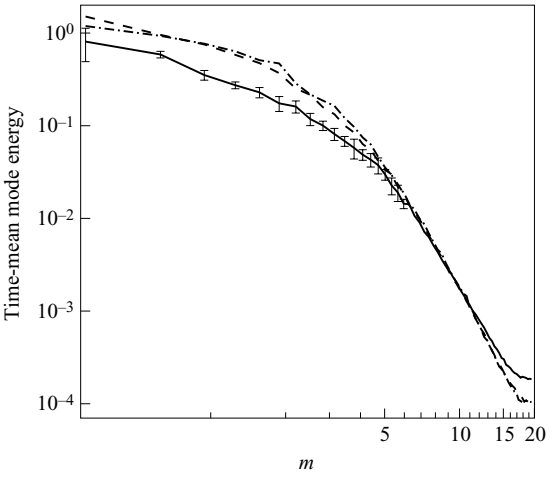


FIGURE 17. Time-averaged mode energy spectrum for wakes behind a square cylinder at $Re = 300$ with a spanwise domain length of $20d$, plotted against wavenumber m. Line styles show incidence angles $\alpha = 0°$ (solid curve), 22.5° (dashed curve) and 45° (dash-dotted curve). A logarithmic scale is used on both axes. Error bars are included with the 0° data over the domain $m < 6$, where the error bar magnitude is determined from the standard deviation of the energy time history for each mode.

spatio-temporal chaos at shorter distances downstream than at smaller incidence angles. The reliability of this interpretation could be questioned due to the relatively small sample set for this data. However, the range of uncertainty for the 0° data (indicated by the error bars showing the standard deviation of each point) is much smaller than the difference between the 0° data and the other data for $m \lesssim 3.5$.

The work presented in this paper provides a clear picture of the transitions in the wake of an inclined square cylinder as the Reynolds number is increased through the three-dimensional transition regime. The onset of three-dimensional flow occurs at Reynolds numbers elucidated in figure 5, which causes the formerly parallel and two-dimensional wake vortices to develop three-dimensional flow through either a mode A or a mode C instability, depending on the incidence angle. Beyond the onset of these instabilities, nonlinear effects and spanwise irregularities can lead to gradual switching between available three-dimensional modes (such as between modes A and C at 15°). The resulting localized phase shifts distort the formerly parallel Kármán vortices. Further downstream, this leads to a wake pattern formation consistent with spatio-temporal chaos, whereby the distorted wake vortices undergo an irregular breakup and merging process. The spatio-temporally chaotic wake replaces the spanwise-periodic shorter wavelength three-dimensional structures associated with the linear instability modes. Streamwise vortices resembling the mode B instability persist in the near wake and coexist with the structures arising from spatio-temporal chaos further downstream. Inferring from computations reported by (Henderson 1997) and experimental studies (e.g. Mansy *et al.* 1994), this behaviour will likely persist beyond $Re = 1000$.

3.7. *Strouhal–Reynolds number dependence*

Attention is now directed to the Strouhal–Reynolds number dependence of inclined square cylinders. Strouhal numbers were determined by recording time histories of velocity at a point in the wake $3d$ directly downstream of the cylinder. Below the

https://doi.org/10.1017/S0022112009006879 Published online by Cambridge University Press

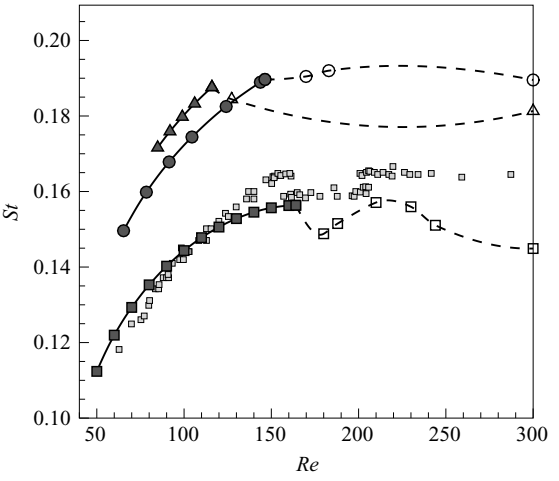


FIGURE 18. A plot of St against Re for a square cylinder at incidence angles (□) 0°, (○) 22.5° and (△) 45°. Filled symbols show data acquired in the two-dimensional regime, while open symbols show data from three-dimensional computations. Solid and dashed Curves are spline fits to aid the eye. Small lightly shaded symbols show experimentally measured data digitized from Tong *et al.* (2008) for a square cylinder at $\alpha = 0°$ for comparison.

transition Reynolds numbers for three-dimensional flow, Strouhal numbers were calculated from two-dimensional simulations, which remained periodic over the range of Reynolds numbers presented here. Three-dimensional computations often saturated to an aperiodic state, and in these cases a mean shedding frequency was calculated by determining the average period over many shedding cycles. The results are plotted in figure 18, with three-dimensional data taken from the short- and long-span simulations reported in § 3.4 and § 3.6, respectively.

Strouhal number data was acquired at $\alpha = 0°$, 22.5° and 45°. In the two-dimensional regime, the results for $\alpha = 0°$ are qualitatively similar to those reported in Robichaux *et al.* (1999), though their results were artificially amplified by the substantially smaller domain: i.e. their blockage ratio was 5.56 %, compared to the present 2.4 %, and their domain extended upstream and downstream just 25 % and 49 % of the lengths used in this study, respectively.

The two-dimensional regime displays a distinctive trend characterized by an increasing St value and decreasing gradient with increasing Reynolds number. This trend is consistent with circular cylinders (Williamson 1988*a*) and slender rings (Leweke & Provansal 1995), and those studies may be consulted for quadratic relationships for the Roshko number ($St\,Re$) as a function of Re. Here the square cylinder produces an increase in Strouhal number with an increase in incidence angle from 0° to 45°. Beyond the onset of three-dimensional flow, limited data is available from the computations, though important features have been captured. These include the pronounced reduction in Strouhal number through the emergence of mode A above $Re = 164$ at $\alpha = 0°$, a subsequent increase in Strouhal number to the level achieved just prior to the development of three-dimensional flow at mode B emerges beyond $Re \approx 200$, and at higher incidence angles, a plateau in Strouhal number beyond three-dimensional transition. It is apparent that the onset of three-dimensional flow initiates a regime exhibiting a reduced Strouhal-number-dependence on Reynolds number.

https://doi.org/10.1017/S0022112009006879 Published online by Cambridge University Press

Included in figure 18 is experimental data digitized from Tong *et al.* (2008) for a square cylinder at $\alpha = 0°$, in close agreement with the present numerical results. The experimental results are greater than the computed results beyond $Re \approx 120$, with a discrepancy of approximately 0.008 in the three-dimensional transition regime. Their experimental setup employed end-plates to maintain uniform parallel shedding in the vortex street, and as documented in Luo *et al.* (2007), they measured an increase in Strouhal number of up to 0.012 as the end-plate angle increased from 0° to 14°. They employed an end-plate angle of 14° for their hot film measurements of Strouhal number, which may account for the discrepancy between these results.

4. Conclusions

This paper describes the three-dimensional transition scenarios in the wake of a square cylinder inclined at angles $0° \leqslant \alpha \leqslant 45°$. In contrast with an earlier study, it is found that the first-occurring three-dimensional wake instability differs depending on incidence angle. The first-occurring instability is mode A for $0° \leqslant \alpha \lesssim 12°$ and $26° \lesssim \alpha \leqslant 45°$, and mode C for $12° \lesssim \alpha \lesssim 26°$. Transition Reynolds numbers Re_{crit} and spanwise perturbation wavelengths λ_{crit}/d were found for each instability mode and these are summarized in figures 5 and 6, respectively. Based on the frontal height of the cylinder, the critical Reynolds numbers for the first-occurring three-dimensional instability varied from $Re_{\text{crit}} = 164$ at $\alpha = 0°$ to $Re_{\text{crit}} = 116$ at $\alpha = 45°$. Consistent with earlier studies (Sheard *et al.* 2003) and theory (Marques *et al.* 2004), the subharmonic mode C instability is most unstable at incidence angles providing the greatest asymmetry about the wake centreline (i.e. $\alpha \approx 20°$–$25°$).

At $\alpha = 0°$, a quasi-periodic mode was detected at wavelengths between those of modes A and B. With increasing incidence angle, shorter wavelength modes, as well as quasi-periodic modes, became less prevalent and were supplanted by the mode C instability. Three-dimensional computations verified the predicted three-dimensional transition modes, and a nonlinear analysis using the Landau equation was used to determine that the mode A instability develops through a supercritical bifurcation at 0° and a subcritical bifurcation at 45°, and the mode C instability develops through a supercritical bifurcation at 22.5°.

With a spanwise domain of $20d$, computations at $Re = 300$ showed that the parallel Kármán vortices break down through the development of spatio-temporal chaos. This development causes the wakes to be dominated by energy in the longest available spanwise wavelengths, rather than the wavelengths associated with the original linear instability modes.

To carry out the computations reported in this study, the resources of the Australian Partnership for Advanced Computing (APAC) were employed thanks to a grant under the Merit Allocation Scheme. The authors thank Associate/Professor Luo Siao Chung and the Journal of Fluids and Structures for granting permission to reproduce part of figure 5 from Tong *et al.* (2008).

Appendix. Loss of symmetry about the wake centreline

In two-dimensional computations at Reynolds numbers $Re \gtrsim 280$ and $\alpha = 45°$, an asymmetry about the wake centreline emerged in the wake. This asymmetry developed independently of spatial resolution, being observed for all element polynomial degrees from 5 to 11. After convecting some distance downstream, the von Kármán vortex

https://doi.org/10.1017/S0022112009006879 Published online by Cambridge University Press

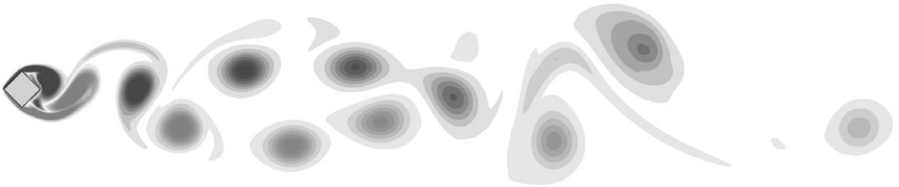


FIGURE 19. A plot showing contours of spanwise vorticity in the wake of a cylinder with $\alpha = 45^\circ$ at $Re = 318$. Notice that the wake deflects downwards, below the geometric centreline, despite the symmetry of the body.

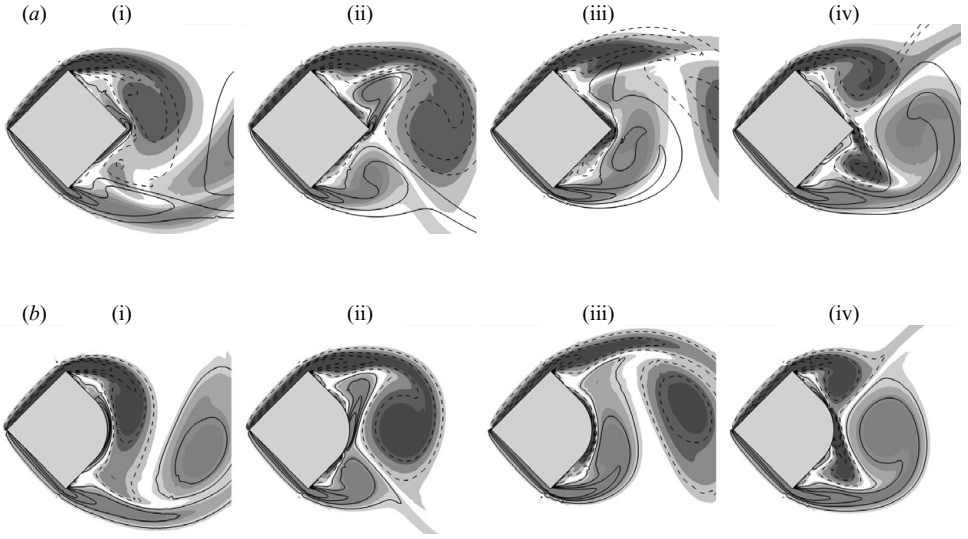


FIGURE 20. Plots of vorticity in the near wake at $Re = 318$ for (a) a square cylinder $\alpha = 45^\circ$, and (b) a cylinder with a rounded trailing edge. Shaded contours show spanwise vorticity at (i) maximum lift, (ii) zero lift (lift decreasing), (iii) minimum lift and (iv) zero lift (lift increasing). Contour lines show vorticity shifted in time by one half-period, and reflected in space about the geometric centreline ($y = 0$). When the contour lines match the shaded contours, the wake is spatio-temporally symmetric about the centreline.

street drifted transversely from the wake centreline (see figure 19). Sohankar *et al.* (1999) mentioned this effect briefly for their two-dimensional simulations around square cylinders at $\alpha = 0^\circ$. However, the focus of that study was three-dimensional flows, and this phenomenon was not investigated in detail.

The pronouncement of the asymmetry was observed to increase with Reynolds number, and the direction of propagation was determined by random initial perturbations in the flow. Here the direction of vortex street propagation remained biased to one side of the wake for at least 50 shedding cycles.

It was hypothesized that this asymmetry developed as a result of an instability of the cyclic separation of flow from the sharp trailing corner of the body. This corner penetrates into the formation region of the wake, and leads to an asymmetric development of wake vortices. This is especially visible in figure 20. Notice, in figure 20(a), the asymmetry in the negative vorticity near the lower aft surface of the cylinder (i), and the corresponding positive vorticity near the upper aft surface (iii).

https://doi.org/10.1017/S0022112009006879 Published online by Cambridge University Press

In order to test this hypothesis, a modified cylinder geometry was constructed featuring a square cylinder at $\alpha = 45°$, but with the downstream corner of the cylinder being rounded, as shown in figure 20(*b*). Comparing the frames in figure 20(*b*) with figure 20(*a*) demonstrates the significant asymmetry in the near wake which develops as a result of the disruption to the flow caused by the sharp trailing edge of the 45° cylinder.

Simulations at $Re = 318$, 354 and 389 were performed using this modified cylinder. The wakes computed behind this modified cylinder exhibited no evidence of the aforementioned asymmetry, and a zero time-averaged lift coefficient was recorded consistently. This confirms that the source of this wake asymmetry is the separating flow from the sharp downstream corner of the square cylinder.

Three-dimensional simulations at these Reynolds numbers were performed to determine if the same asymmetry emerged. Interestingly, the development of three-dimensional flow in the wake acted to suppress this asymmetry. Therefore, at least for this geometry, it is expected that this asymmetry will not be detected experimentally, though it remains an open question as to whether this holds for all bodies which exhibit this phenomenon.

In a number of cases, wake vortices were found to coalesce into two parallel shear layers of opposite-sign vorticity. Further downstream, these shear layers became unstable and a second vortex street was produced. This phenomenon was observed for $Re \gtrsim 70$. This far-wake phenomenon is well known, having been studied numerically and experimentally (Taneda 1959; Williamson & Prasad 1993; Karasudani & Funakoshi 1994; Inoue & Yamazaki 1999), and thus is not further investigated here.

REFERENCES

Barkley, D. & Henderson, R. D. 1996 Three-dimensional Floquet stability analysis of the wake of a circular cylinder. *J. Fluid Mech.* **322**, 215–241.

Blackburn, H. M. & Lopez, J. M. 2003 On three-dimensional quasi-periodic Floquet instabilities of two-dimensional bluff body wakes. *Phys. Fluids* **15** (8), L57–L60.

Blackburn, H. M. & Sherwin, S. J. 2004 Formulation of a Galerkin spectral element-Fourier method for three-dimensional incompressible flow in cylindrical geometries. *J. Comput. Phys.* **197**, 759–778.

Carmo, B. S., Sherwin, S. J., Bearman, P. W. & Willden, R. H. J. 2008 Wake transition in the flow around two circular cylinders in staggered arrangements. *J. Fluid Mech.* **597**, 1–29.

Dutta, S., Panigrahi, P. K. & Muralidhar, K. 2008 Experimental investigation of flow past a square cylinder at an angle of incidence. *J. Engng Mech.-ASCE* **134** (9), 788–803.

Henderson, R. D. 1997 nonlinear dynamics and pattern formation in turbulent wake transition. *J. Fluid Mech.* **352**, 65–112.

Henderson, R. D. & Barkley, D. 1996 Secondary instability in the wake of a circular cylinder. *Phys. Fluids* **8**, 1683–1685.

Inoue, O. & Yamazaki, T. 1999 Secondary vortex streets in two-dimensional cylinder wakes. *Fluid Dyn. Res.* **25** (1), 1–18.

Karasudani, T. & Funakoshi, M. 1994 Evolution of a vortex street in the far wake of a circular cylinder. *Fluid Dyn. Res.* **14** (6), 331–352.

Karniadakis, G. E., Israeli, M. & Orszag, S. A. 1991 High-order splitting methods for the incompressible Navier–Stokes equations. *J. Comput. Phys.* **97**, 414–443.

Karniadakis, G. E. & Triantafyllou, G. S. 1992 Three-dimensional dynamics and transition to turbulence in the wake of bluff objects. *J. Fluid Mech.* **238**, 1–30.

Landau, L. D. & Lifshitz, E. M. 1976 *Mechanics. Third Edition*. Pergamon Press.

Lehoucq, R. B., Sorenson, D. C. & Yang, C. 1998 *ARPACK Users' Guide*. SIAM.

https://doi.org/10.1017/S0022112009006879 Published online by Cambridge University Press

Leweke, T. & Provansal, M. 1994 Model for the transition in bluff body wakes. *Phys. Rev. Lett.* **72** (20), 3174–3177.

Leweke, T. & Provansal, M. 1995 The flow behind rings: bluff body wakes without end effects. *J. Fluid Mech.* **288**, 265–310.

Leweke, T. & Williamson, C. H. K. 1998 Cooperative elliptic instability of a vortex pair. *J. Fluid Mech.* **360**, 85–119.

Luo, S. C., Chew, Y. T. & Ng, Y. T. 2003 Characteristics of square cylinder wake transition flows. *Phys. Fluids* **15** (9), 2549–2559.

Luo, S. C., Tong, X. H. & Khoo, B. C. 2007 Transition phenomena in the wake of a square cylinder. *J. Fluids Struct.* **23**, 227–248.

Mansy, H., Yang, P.-M. & Williams, D. R. 1994 Quantitative measurements of three-dimensional structures in the wake of a circular cylinder. *J. Fluid Mech.* **270**, 277–296.

Marques, F., Lopez, J. M. & Blackburn, H. M. 2004 Bifurcations in systems with Z_2 spatio-temporal and $O(2)$ spatial symmetry. *Physica* D **189** (3/4), 247–276.

Mittal, R. & Balachandar, S. 1996 Direct numerical simulation of flow past elliptic cylinders. *J. Comput. Phys.* **124**, 351–367.

Ranjan, R., Dalal, A. & Biswas, G. 2008 A numerical study of fluid flow and heat transfer around a square cylinder at incidence using unstructured grids. *Numer. Heat Transfer* A-*Appl.* **54** (9), 890–913.

Robichaux, J., Balachandar, S. & Vanka, S. P. 1999 Three-dimensional Floquet instability of the wake of a square cylinder. *Phys. Fluids* **11** (3), 560–578.

Ryan, K., Thompson, M. C. & Hourigan, K. 2005 Three-dimensional transition in the wake of bluff elongated cylinders. *J. Fluid Mech.* **538**, 1–29.

Saha, A. K., Biswas, G. & Muralidhar, K. 2003 Three-dimensional study of flow past a square cylinder at low Reynolds numbers. *Intl J. Heat Fluid Flow* **24**, 54–66.

Sheard, G. J. 2009 Cylinders with elliptical cross-section: wake stability with variation in angle of incidence. In *IUTAM Symposium on Unsteady Separated Flows and their Control* (ed. M. Braza & K. Hourigan), Proceedings of the IUTAM Symposium "Unsteady Separated Flows and their Control", Corfu, Greece, 18–22 June 2007, IUTAM Bookseries. Vol. 14, ISBN: 978-1-4020-9897-0.

Sheard, G. J., Leweke, T., Thompson, M. C. & Hourigan, K. 2007 Flow around an impulsively arrested circular cylinder. *Phys. Fluids* **19** (8), 083601.

Sheard, G. J. & Ryan, K. 2007 Pressure-driven flow past spheres moving in a circular tube. *J. Fluid Mech.* **592**, 233–262.

Sheard, G. J., Thompson, M. C. & Hourigan, K. 2003 From spheres to circular cylinders: the stability and flow structures of bluff ring wakes. *J. Fluid Mech.* **492**, 147–180.

Sheard, G. J., Thompson, M. C. & Hourigan, K. 2004 From spheres to circular cylinders: non-axisymmetric transitions in the flow past rings. *J. Fluid Mech.* **506**, 45–78.

Sheard, G. J., Thompson, M. C., Hourigan, K. & Leweke, T. 2005 The evolution of a subharmonic mode in a vortex street. *J. Fluid Mech.* **534**, 23–38.

Shraiman, B. I., Pumir, A., van Saarloos, W., Hohenberg, P. C. & Chaté, H. 1992 Spatiotemporal chaos in the one-dimensional complex Ginzburg–Landau equation. *Physica* D **57** (3–4), 241–248.

Sohankar, A., Norberg, C. & Davidson, L. 1999 Simulation of three-dimensional flow around a square cylinder at moderate Reynolds numbers. *Phys. Fluids* **11** (2), 288–306.

Taneda, S. 1959 Downstream development of wakes behind cylinders. *J. Phys. Soc. Jpn* **14** (6), 843–848.

Thompson, M. C., Hourigan, K. & Sheridan, J. 1996 Three-dimensional instabilities in the wake of a circular cylinder. *Exp. Therm. Fluid Sci.* **12**, 190–196.

Thompson, M. C., Leweke, T. & Provansal, M. 2001*a* Kinematics and dynamics of sphere wake transition. *J. Fluids Struct.* **15**, 575–585.

Thompson, M. C., Leweke, T. & Williamson, C. H. K. 2001*b* The physical mechanism of transition in bluff body wakes. *J. Fluids Struct.* **15**, 607–616.

Tong, X. H., Luo, S. C. & Khoo, B. C. 2008 Transition phenomena in the wake of an inclined square cylinder. *J. Fluids Struct.* **24** (7), 994–1005.

https://doi.org/10.1017/S0022112009006879 Published online by Cambridge University Press

Williamson, C. H. K. 1988*a* Defining a universal and continuous Strouhal–Reynolds number relationship for the laminar vortex shedding of a circular cylinder. *Phys. Fluids* **31**, 2742–2744.

Williamson, C. H. K. 1988*b* The existence of two stages in the transition to three-dimensionality of a cylinder wake. *Phys. Fluids* **31**, 3165–3168.

Williamson, C. H. K. 1992 The natural and forced formation of spot-like 'vortex dislocations' in the transition of a wake. *J. Fluid Mech.* **243**, 393–441.

Williamson, C. H. K. 1996 Three-dimensional wake transition. *J. Fluid Mech.* **328**, 345–407.

Williamson, C. H. K. & Prasad, A. 1993 Wave interactions in the far wake of a body. *Phys. Fluids* A-*Fluid Dyn.* **5** (7), 1854–1856.

Wu, J., Sheridan, J., Welsh, M. C. & Hourigan, K. 1996 Three-dimensional vortex structures in a cylinder wake. *J. Fluid Mech.* **312**, 201–222.

Zhang, H., Noack, B. R., König, M. & Eckelmann, H. 1995 On the transition of the circular cylinder wake. *Phys. Fluids* **7** (4), 779–793.

https://doi.org/10.1017/S0022112009006879 Published online by Cambridge University Press